

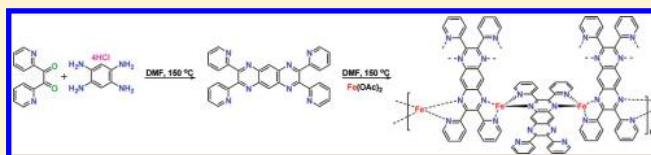
# Heat-Treated Nonprecious Catalyst Using Fe and Nitrogen-Rich 2,3,7,8-Tetra(pyridin-2-yl)pyrazino[2,3-g]quinoxaline Coordinated Complex for Oxygen Reduction Reaction in PEM Fuel Cells

Jason Wu,<sup>†</sup> Wenmu Li,<sup>†</sup> Drew Higgins, and Zhongwei Chen\*

Department of Chemical Engineering, Waterloo Institute for Nanotechnology, Waterloo Institute for Sustainable Energy, University of Waterloo, Waterloo, Ontario, N2L 3G1, Canada

Supporting Information

**ABSTRACT:** Pyrolyzed Fe/N/C catalysts were synthesized using a newly designed and synthesized 2,3,7,8-tetra(pyridin-2-yl)pyrazino[2,3-g]quinoxaline (TPPQ) organic compound as the nitrogen-containing ligand. The structure of TPPQ was deliberately designed to discourage the agglomeration of Fe during heat treatment as well as to provide a concentrated source of nitrogen. Catalysts were prepared by first coordinating TPPQ with Fe, forming Fe–TPPQ complexes, followed by impregnation onto carbon black (KJ600) and pyrolysis at 900 °C. Catalysts with 0.5%, 1%, 2%, 4%, and 8% initial iron content were prepared, and their physical characteristics were determined by X-ray diffraction, transmission electron microscopy, and X-ray photoelectron spectroscopy analysis. Electrocatalytic activity toward the oxygen reduction reaction was evaluated and compared for all catalysts. The best performing catalyst was found to be the catalyst using 2% initial iron content. Evidence of iron metal and carbide particle formation was found for catalysts with initial iron content higher than 2%.



## INTRODUCTION

Polymer electrolyte membrane (PEM) fuel cells have garnered widespread attention due to their potential application as stationary, mobile, and transportation power devices. The sluggish oxygen reduction reaction (ORR) kinetics occurring at the cathode is considered the primary limiting factor facing the performance of these devices. As of now, platinum-based catalysts are the only commercially available option that show the best performance and stability under the harsh acidic conditions encountered at the cathode. The excessive cost and limited supply of platinum hinders the economical feasibility of these devices. Two approaches can be taken to offset the high cost of platinum; (1) increase platinum utilization at the cathode in order to reduce the overall platinum requirement,<sup>1,2</sup> or (2) completely replace platinum by nonprecious metal alternatives.<sup>3–5</sup> In the long term, due to limited supply of platinum, it is more desirable to develop non-platinum, nonprecious catalysts.

Research in transition metal organic complexes as nonprecious ORR catalyst alternatives began in the 1960s<sup>3</sup> with the investigation of transition metal macrocyclic complexes. Later studies indicated that the pyrolysis of these transition metal macrocycles could lead to significant improvement in both activity and stability.<sup>4–10</sup> Drawing on this, a significant breakthrough was achieved years later when researchers demonstrated the potential of creating active catalyst materials by pyrolysis methods without the use of expensive macrocyclic precursors.<sup>10–12</sup> These active catalysts were synthesized through the pyrolysis of separate nitrogen, carbon, and transition metal precursors, resulting in a promising class of M–N/C catalysts (M = Fe, Co). Although the

nonpyrolyzed macrocycles provide the added benefit of structural control, these nonpyrolyzed catalysts suffer from lower activity and lower stability when compared to their heat-treated counterparts.<sup>13</sup> The heat treatment of M–N/C catalysts provides the necessary stability and catalytic activity<sup>4,9,14–17</sup> needed in acidic conditions at the cost of facile structural control and active site determination.

The nature of the ORR active site moieties for pyrolyzed nonprecious M–N/C catalysts in acid solution is under constant debate. It is still unknown whether the transition metal center acts as the locale for catalytic activity or whether the transition metal merely catalyzes the formation of active nitrogen–carbon functionalities.<sup>9,10,15,18–23</sup> Regardless, the combination of a transition metal, nitrogen, and a carbon source is required to create active catalysts. Among the transition metals used, iron has been shown to result in catalysts with the highest catalytic activity toward the oxygen reduction reaction.<sup>5,15,19,24,25</sup> In most cases, the nitrogen precursor is an organic carbon containing compound,<sup>15,17,25–34</sup> although success with catalysts using gaseous nitrogen precursors has also been observed.<sup>23,35–38</sup>

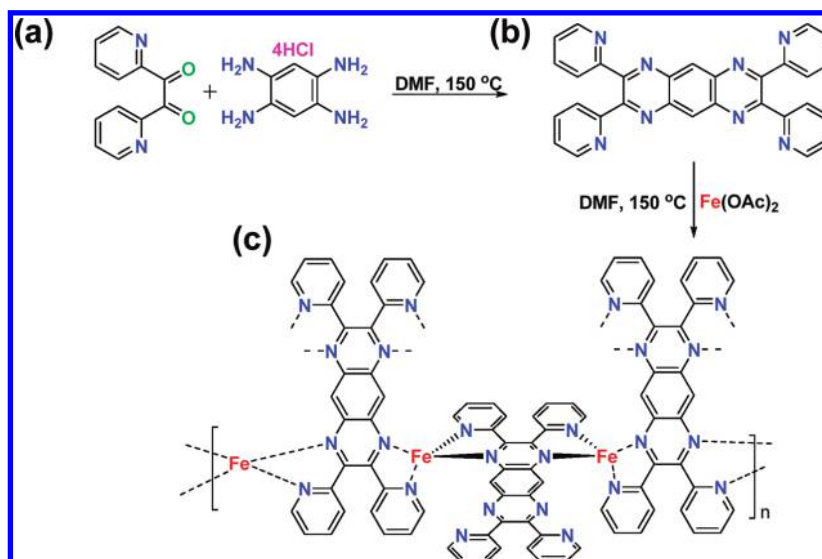
The choice of nitrogen precursor greatly affects the resulting activity of the catalyst. Currently, the study of Fe–N/C heat-treated catalysts has mainly focused on using commercially available nitrogen precursors such as phthalocyanines,<sup>25,30,34</sup> porphyrins,<sup>39–41</sup> ethylenediamine,<sup>27,28</sup> polyaniline,<sup>17,31</sup> cyanamide,<sup>29,32</sup> TPTZ,<sup>33</sup> NH<sub>3</sub>,<sup>35,36</sup> and acetonitrile.<sup>23,37,38</sup> There exist a number of challenges

Received: May 24, 2011

Revised: August 18, 2011

Published: August 19, 2011

Scheme 1. Synthesis of TPPQ and Associated Iron-Complex Polymers



arising from the heat treatment of iron and the available nitrogen precursors. Phthalocyanines and porphyrins as nitrogen sources have been found to produce active catalysts; however, these expensive macrocycles are limited in use by their high cost. As for low cost nitrogen precursors such as ethylenediamine, polyaniline, cyanamide, and NH<sub>3</sub>, these precursors do not naturally create uniformly distributed Fe–N type sites prior to pyrolysis as is in the case with the macrocycles. Two additional challenges surface in parallel with the added benefits of high temperature pyrolysis that apply to all commercially available nitrogen precursors. Sintering, the formation of large metal iron particles, is inevitable,<sup>14,25,33</sup> and the loss of active nitrogen in the system. In both cases, the hindering of active site formation is a possibility. It is possible to address these challenges by designing a new low-cost nitrogen precursor that easily coordinates with iron, creating well-distributed Fe–N sites prior to pyrolysis. A potential method to discourage the formation of large iron particles is to synthesize a low cost Fe–N-ligand complex with well-isolated iron sites prior to pyrolysis. Furthermore, an iron–nitrogen complex containing high nitrogen content will effectively increase the degree of iron–nitrogen coordination, providing an ideal template structure for active site formation prior to pyrolysis.

Taking into account the above-mentioned challenges and potential solutions for heat-treated Fe-based catalysts, in the present work, a novel, nitrogen-rich monomer 2,3,7,8-tetra-(pyridin-2-yl)pyrazino[2,3-g]quinoxaline (TPPQ) was designed and synthesized. The nitrogen-rich ligand was synthesized using a single-step reaction (Scheme 1a), and it consists of almost 22 wt % of highly thermally stable pyridinic nitrogen. Stable pyridinic nitrogen is used in the structure with the intention of promoting facile active site formation and allowing for a high degree of Fe–N coordination at high pyrolysis temperature. The nitrogen-rich ligand (Scheme 1b) was then coordinated with iron, forming an ionomer-like complex consisting of alternating chains of ligand and iron as seen in Scheme 1c to be used as the carbon black pore filler. The formation of an iron–ligand ionomer is a necessity to ensure that the iron sites in the system remain secluded and well isolated from one another, impeding agglomeration of iron and facilitating well-distributed active site formation. Furthermore, the triple aromatic ring structure in the center

of the monomer is also highly thermally stable, allowing the monomer to remain as a spacer between iron sites during pyrolysis. In addition, aromatic structures in the ligand help promote the formation of graphitized carbon on the surface of the carbon support, which can potentially be beneficial for the activity of the catalyst.<sup>17</sup> Due to the thermally stable aromatic and pyridinic structures present in the ligand, the ligand is thought to be capable of accommodating a higher concentration of iron during synthesis in the attempt to create more active sites. On the basis of this ligand, an electrochemically active catalyst is synthesized after heat treatment, and its activity is evaluated. Further analysis on the physical characteristics of the catalyst via X-ray photoelectron spectroscopy (XPS), X-ray diffraction (XRD), and transmission electron microscopy (TEM) analysis was also conducted.

## EXPERIMENTAL METHODS

**TPPQ Ligand Synthesis.** Synthesis of the nitrogen-rich ligand is carried out using 2,2'-pyridyl (Sigma-Aldrich) and 1,2,4,5-benzenetetramine tetrahydrochloride (Sigma-Aldrich). An overview of the synthesis reaction can be found in Scheme 1. Synthesis begins with suspending 0.60 g (1.64 mmol) of 2,2'-pyridyl and 0.088 g (0.82 mmol) of 1,2,4,5-benzenetetramine tetrahydrochloride in 3 mL of DMF. Both solutions are then mixed together, heated to 150 °C, and refluxed for a total of 1 h. Finally, the mixture is allowed to cool to room temperature and then filtered using a microporous filter and a qualitative filter paper. The filtrate is then allowed to dry overnight.

**Catalyst Synthesis.** Catalysts were synthesized and tested for catalytic activity with initial iron loadings of 0.5, 1, 2, 4, and 8 wt %, respectively. In the case of the 1% iron loading, 10 mg of the ligand monomer was dissolved in 20 mL of DMF and then purged with nitrogen. A solution of 3.5 mg of iron(II) acetate in 2 mL of ethanol is then prepared and sonicated. While under protection of nitrogen, the solution of iron(II) acetate was added dropwise into the ligand and DMF mixture at 150 °C. The reaction is then allowed to proceed for 1 h before 100 mg of acid-treated carbon black (Ketjen Black EC600) was added, and then the mixture was allowed to sit for another hour. The resulting

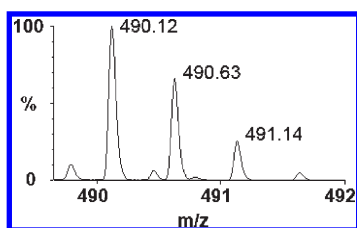


**Figure 1.** Electron ionization (EI) mass spectrometry spectrum of TPPQ nitrogen-rich ligand, indicating  $m/z$  major peaks at 490.12, 490.62, and 491.14  $m/z$ .

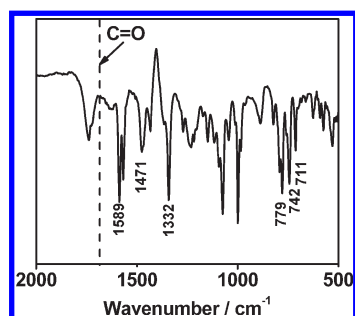


**Figure 2.** FTIR spectrum of TPPQ nitrogen-rich ligand, showing key pyridinic peaks at 1589, 1471, and 1332  $\text{cm}^{-1}$ , corresponding to ring stretching vibrations associated with the C=N and C=C ring stretching, and at 711, 742, and 779  $\text{cm}^{-1}$ , corresponding to out-of-plane C-H bending. The characteristic doublet peaks at 1717 and 1695  $\text{cm}^{-1}$  pertaining to C=O vibrations in 2,2'-pyridyl are not found in the final product.

mixture is then poured into 200 mL of distilled water to precipitate out the catalyst which is then filtered, collected, and dried overnight. Finally, the dried sample is heated to 900 °C for 1 h at a heating ramp rate of 10 °C  $\text{min}^{-1}$ . The synthesis procedure was repeated for initial iron loading by varying the mass of iron(II) acetate accordingly.

**Physical Characterization.** The characteristic functional groups of the nitrogen-containing precursor were confirmed to be present by analyzing an IR spectrum obtained from a Bruker Tensor Series FTIR spectrometer. An NMR spectrum of the synthesized ligand was taken with a Bruker AVANCE-300 NMR spectrometer with the ligand dissolved in  $\text{CDCl}_3$ . Surface morphology of the catalyst was examined via images digitally taken from a JEOL2010F Field Emission STEM. Catalysts were dispersed in methanol before a single drop was deposited onto a support mesh, creating a thin film. Evidence of iron particle formation was verified using a Bruker D8 XRD. XPS analysis of the samples was performed using a Thermo Scientific K-Alpha XPS spectrometer. The samples were run at a takeoff angle of 90° using an Al K $\alpha$  X-ray source with a spot area of 400  $\mu\text{m}$ .

**ORR Activity Evaluation.** Electrochemical activity of the catalyst was determined using a rotating ring disk electrode (RRDE). A catalyst ink was prepared by dissolving 2 mg of the catalyst into 1 mL of a solution containing Nafion, ethanol, and water. Twenty microliters of the catalyst ink was then deposited on a glassy carbon electrode with a surface area of 0.196  $\text{cm}^2$  with an overall catalyst loading of 0.2  $\text{mg}/\text{cm}^2$ . The working electrode with the deposited catalyst was used in a three-electrode cell setup with a platinum counter electrode, an Ag/AgCl reference electrode, and with 0.1 M perchloric acid as the electrolyte. After

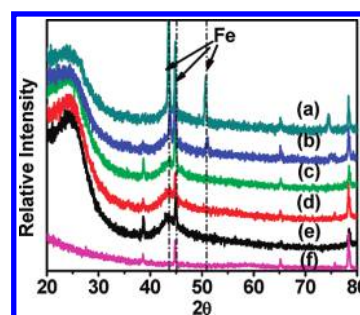


**Figure 3.** XRD spectra of catalyst samples with (a) 8%, (b) 4%, (c) 2%, (d) 1%, and (e) 0.5% initial iron percent and (f) sample holder. Evidence of iron particle formation can be seen by peaks at 44°, 45°, and 51° for 4% and 8% Fe catalysts.

the electrolyte was saturated with oxygen, currents were measured by linearly sweeping the potential from  $-0.28$  to  $0.95$  V against Ag/AgCl at 100, 400, 900, and 1600 rpm rotation rates.

## RESULTS AND DISCUSSION

Synthesis of the nitrogen-rich ligand, TPPQ, can be depicted in Scheme 1, using a direct reaction between 2,2'-pyridyl and 1,2,4,5-benzenetetramine tetrahydrochloride. To confirm the structure of TPPQ, electron ionization (EI) mass spectrometry (Figure 1), FTIR spectroscopy (Figure 2), and NMR spectroscopy were performed (Figure S2, Supporting Information). The results from EI mass spectrometry shows a set of peaks at 490.1187  $m/z$ , 490.6308  $m/z$ , and 491.1269  $m/z$ , with the largest peak centered at 490.1187  $m/z$  (Figure 1). These peaks centered at the aforementioned  $m/z$  ratios closely correspond to the expected molecular weight of the precursor at 490.52 g/mol. Further characterization of the structure of the precursor by FTIR spectroscopy shows key peaks at 1589, 1471, and 1332  $\text{cm}^{-1}$  which correspond to the ring stretching vibrations associated with the C=N and C=C ring stretching, and at 779, 742, and 711  $\text{cm}^{-1}$  which corresponds to the out-of-plane C-H bending (Figure 2). Additionally, it can be seen that the characteristic carbonyl doublet peaks at 1717 and 1695  $\text{cm}^{-1}$  of 2,2'-pyridyl disappears in the spectrum of the synthesized ligand, further confirming the formation of TPPQ.<sup>42</sup> These peaks identify the pyridinic nitrogen groups which are the key aspects of the precursor.

The overall catalytic activity of a catalyst can be increased either by improving upon its intrinsic active site turnover frequency or by increasing the surface density of active sites. Taking the stance that the catalytic site exists in some form on graphitic edge planes as a result of iron and nitrogen,<sup>15,21</sup> it can be logically declared that higher concentrations of iron will result in higher concentrations of active sites. Of course, the consequence of increasing iron content is the saturation of nitrogen sites and the eventual formation of metal or carbide iron particles. As previously discussed, the design of TPPQ is intended on increasing the density of active sites by allowing for higher iron loadings while discouraging the formation of large iron particles. In this case, a reasonable benchmark in gauging the efficacy of the new catalyst is to determine the existence of large iron particles after heat treatment. To do so, XRD and TEM surface analysis was utilized to confirm the existence of agglomerated iron metal or carbide iron. The XRD spectrum of catalysts with different initial iron loadings can be seen in Figure 3. From Figure 3, it is

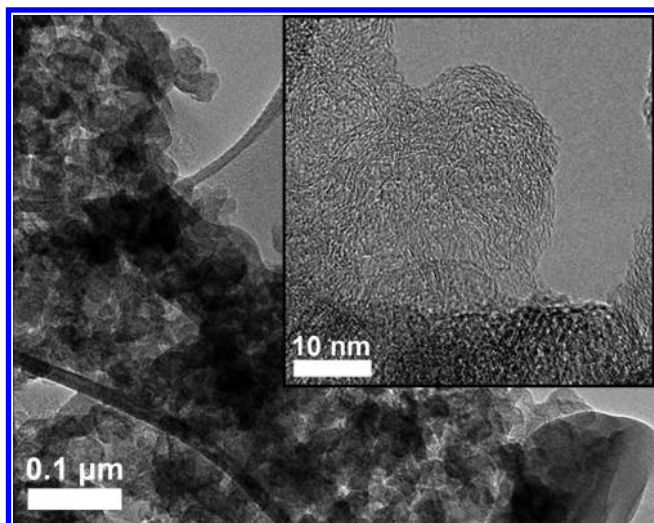


Figure 4. TEM micrographs of catalyst with 2% initial Fe weight percent.

possible to see the emergence of three distinct key peaks signifying iron particle formation at  $44^\circ$ ,  $45^\circ$ , and  $51^\circ$  as the iron content increases.<sup>14,25,33</sup> These three peaks indicate the formation of large iron particles, in particular, the formation of  $\alpha$ -Fe. A strong, distinct peak was observed in the 4% and 8% iron catalysts, indicating the formation of highly crystalline iron particles. In the case of the 2% iron catalyst, the same strong and defined peaks that indicate iron particle formation were not observed. The lack of iron particle formation in the catalyst with 2% iron loading is further emphasized with TEM images as seen in Figure 4. The TEM images of the catalyst shows the expected graphitic structure due to heat treated carbon black, while showing no evidence of iron particle formation of any kind. For the catalysts with higher initial iron loadings, large iron particle formations can be distinctively seen and are shown in the TEM images in Figure S2 in the Supporting Information. On the basis of the results from XRD characterization and TEM imaging, it can be seen that our nitrogen-rich ligand is capable of preventing agglomeration of iron up to an initial iron weight percent of 2%. However, higher iron loadings, still result in large iron particle formation.

The Fe  $2p_{3/2}$  spectra of all synthesized catalysts were examined and are shown in Figure 5. At all initial iron loadings, distinct peak(s) can be found in the Fe  $2p_{3/2}$  region, which indicates the presence of iron in all of the examined catalysts. The oxidation states of surface iron can be interpreted from the spectra, where inactive iron carbides or Fe(0)<sup>19,20,43</sup> can be found at 706.7–706.9 and 706.7–707.2 eV, respectively, Fe(II) at 707.1–708.7 eV, and Fe(III) at 710.8–711.8 eV.<sup>33,43</sup> The median values of the nonionic and ionic iron species are indicated by the vertical dashed lines in Figure 5. A distinct shift toward lower binding energies can be seen in the spectra with increasing initial iron loading. At initial iron loadings of 4% and 8%, a new feature corresponding to iron carbides and Fe(0) appears, likely indicating the appearance of iron aggregates. The iron aggregate feature in the 4% case is slightly shifted toward higher binding energies as is consistent with the overall trend. The additional iron carbide and Fe(0) feature agrees well with previous XRD and TEM results showing the formation of iron particles at the 4% and 8% initial iron loadings. Additionally, in all catalysts, distinct peaks can be found in the Fe(III) region, indicating the

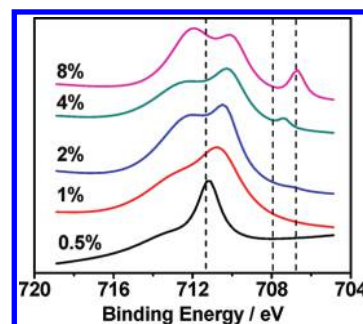


Figure 5. Comparison of XPS Spectra in the Fe  $2p_{3/2}$  region between catalysts with initial iron loadings from 0.5% to 8%.

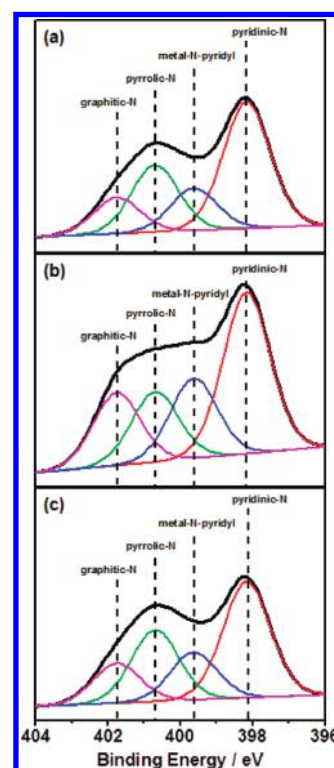
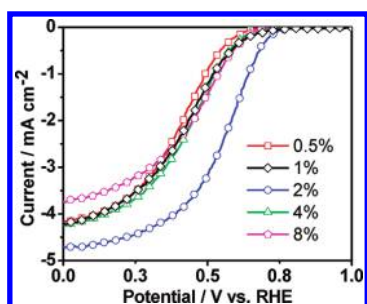


Figure 6. Comparison of XPS spectra in the N 1s region between (a) 1%, (b) 2%, and (c) 4% initial iron loading catalysts. Both 1% and 4% catalysts show a relative increase in graphitic nitrogen content compared to the 2% catalyst.

presence of oxidized iron species in the catalysts. The Fe(III) peak dominates in all catalysts, which suggest that the majority of surface iron exists in an ionic state. These surface iron ions could potentially be the metal species bound to nitrogen as indicated in the N 1s scans.

The discussion of catalytic activity is often associated with the electronic structure of nitrogen. The electronic structure of nitrogen within the graphitic carbon plays an important role in the activity of the catalyst. To better explain the resulting activities of the catalysts, XPS analysis was performed to identify the relative composition of nitrogen and iron in the graphitic system. The N 1s XPS spectra of three catalysts with different initial iron content, 1%, 2%, and 4%, are shown in Figure 6. From the resulting spectra and its fitted peaks, it is possible to identify four peaks related to the different states of nitrogen: pyridinic



**Figure 7.** Comparison of activities between 0.5%, 1%, 2%, 4%, and 8% initial iron loading catalysts at 900 rpm in 0.1 M HClO<sub>4</sub> electrolyte. The most active catalyst is achieved with an initial iron content of 2%.

nitrogen at 398.2 eV, metal–nitrogen at 399.6 eV, pyrrolic nitrogen at 400.7 eV, and graphitic or oxidized nitrogen at 401.8 eV.<sup>23,44,45</sup> Comparing the three catalysts, it is possible to see that both the 1% and 4% catalysts resulted in a loss of both the metal-bound nitrogen and the pyridinic nitrogen identified by the reduced metal-*N*-pyridyl and pyridinic peaks. The difference in peak intensities indicates that for 1% and 4% catalysts less nitrogen exists in both the M–N<sub>x</sub> state and pyridinic state compared to the 2% catalyst case. The relative higher proportion of M–N<sub>x</sub> and pyridinic nitrogen in the 2% iron catalyst suggests that the 2% iron catalyst could contain a higher density of active sites. Additionally, pyridinic nitrogen indicates a higher proportion of exposed graphitic edge planes where the active sites are located.<sup>15,21–23</sup> Since pyridinic nitrogen exists on the edge of graphitic planes, a higher proportion of pyridinic nitrogen coupled with evidence of increased M–N<sub>x</sub> states signify a higher volume and density of exposed active sites; thus it is not unexpected for the 2% catalyst to be the most active among the three.

The catalytic activities of all five catalysts are evaluated using linear sweep voltammetry in a three electrode cell, using 0.1 M HClO<sub>4</sub> as the electrolyte solution. The polarization curves comparing the activities of each catalyst shown in Figure 7 are consistent with our XPS results, with the most active catalyst to be the catalyst with the most iron content while avoiding iron particle formation at 2% initial iron loading. The 2% iron loading catalyst with the best ORR performance as seen in Figure 7 displayed a half-wave potential of 0.52 V vs RHE with a 4.7 mA cm<sup>-2</sup> limiting current at a rotation rate of 900 rpm. As stressed a number of times, it is believed that the transition metal along with nitrogen is a key aspect in providing catalytic activity; thus it is not irrational to expect higher iron content catalysts to provide a higher surface density of active site structures. Higher iron content suggests that more iron is capable of coordinating with the available nitrogen atoms in the system, especially with the use of a highly nitrogen-rich precursor. At the highest of loadings, the formation and agglomeration of the iron particles negatively affect the catalytic performance, whereas at lower iron loadings, the formation of active sites has yet to be fully saturated.

The cases of lower and higher initial iron content deviating from 2% resulted in relatively lower metal-bound and pyridinic nitrogen. The observed lower concentration of metal-bound and pyridinic nitrogen could be the result of two cases of (a) lower and (b) higher initial iron content: (a) When the initial iron content is lower than optimal, there is insufficient iron present in the system to saturate the available nitrogen sites and hold the coordination of the ligands in place. (b) Once the iron content has exceeded an optimal, saturated value, agglomeration of iron

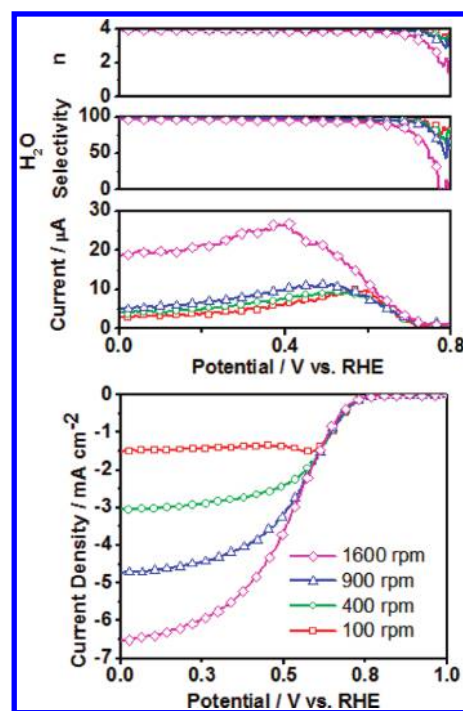


**Figure 8.** Polarization curve and associated ring currents, *n*, and H<sub>2</sub>O selectivity of 2% initial iron content catalyst in 0.1 M HClO<sub>4</sub> in O<sub>2</sub> saturated conditions.

occurs and results in the loss of the coordination between iron and the ligands. The comparison of results obtained for (a) lower and (b) higher iron loadings to that of an optimal initial loading suggests that the use of an optimal initial loading allows for a 2-fold benefit of forming more active sites and exposing more graphitic edges after pyrolysis. Assuming the nature of the active site and the intrinsic activity of the active site remains constant with different initial iron content, the consequence of using a nonoptimal initial iron loading not only suggests a decrease in active site density as seen from the ORR evaluation and N 1s XPS spectra but can also suggest a decrease in exposed graphitic edge planes as implied by the N 1s XPS spectra. As some form of active site exists at the graphitic edges of the micropores,<sup>15,21–23</sup> the decrease in exposed graphitic edge planes is synonymous with the reduction in active site density, and the results agree well.

The associated ring currents and analysis of the ring currents for the 2% initial iron loading catalyst can also be seen in Figure 8. From these figures, it is possible to see that the catalysis of oxygen reduction proceed along a four electron pathway. The number of electrons, *n*, calculated from the ring currents can be seen in Figure 8 along with the H<sub>2</sub>O selectivity. Both *n* and H<sub>2</sub>O selectivity were calculated via analysis of the ring and disk currents with the equations

$$n = 4 \frac{I_D}{I_D + \left(\frac{I_R}{N}\right)}$$

$$H_2O \text{ selectivity} = \frac{I_D - \left(\frac{I_R}{N}\right)}{I_D + \left(\frac{I_R}{N}\right)} \times 100\%$$

where  $I_D$  is the disk current,  $I_R$  is the ring current, and  $N$  is a constant used to account for the ring current collection efficiency. The calculated  $n$  and H<sub>2</sub>O selectivity values approach 4 and 100%, respectively, which provide indication that the catalysis mainly proceeds along a four electron transfer pathway.

## CONCLUSION

In the present work, we have shown the potential and possibilities of designing a nitrogen-rich ligand, TPPQ with deliberate structural control to discourage agglomeration of iron in heat-treated catalysts. The ligand we have designed contains stable carbon structures even at high temperatures which will prevent facile diffusion of iron during pyrolysis. Furthermore, the ligand is unlikely to stack and will form ligand–iron complexes prior to pyrolysis, thus allowing for well-isolated active transition metal sites. We have shown the potential of the ligand in reducing iron agglomeration during pyrolysis, thereby allowing for increased iron content in the hopes of creating more active sites. The ligand's ability to provide well isolated iron sites prior to pyrolysis is confirmed by XRD, TEM, and electrochemical single cell results which show the best performing catalyst to be the catalyst with the most iron content prior to iron particle formation. Additionally, at this saturated iron loading, evidence of an increase proportion of M–N<sub>x</sub> and pyridinic nitrogen is observed and suggests that an optimal initial iron loading may result in a higher density and higher volume of exposed graphitic edge planes.

## ASSOCIATED CONTENT

**S** Supporting Information. NMR spectra of TPPQ (Figure S1) and TEM images of 4% and 8% iron catalysts (Figure S2), showing evidence of large iron metal particle formation. This material is available free of charge via the Internet at <http://pubs.acs.org>.

## AUTHOR INFORMATION

### Corresponding Author

\*E-mail: [zhwchen@uwaterloo.ca](mailto:zhwchen@uwaterloo.ca).

### Author Contributions

<sup>†</sup>Both authors contributed equally to the present work.

## ACKNOWLEDGMENT

This work was financially supported by the Natural Sciences and Engineering Research Council of Canada (NSERC) and the University of Waterloo.

## REFERENCES

- (1) Saha, M. S.; Li, R.; Sun, X.; Ye, S. *Electrochem. Commun.* **2009**, *11*, 438.
- (2) Higgins, D. C.; Meza, D.; Chen, Z. *J. Phys. Chem. C* **2010**, *114*, 21982.
- (3) Jasinski, R. *Nature* **1964**, *201*, 1212.
- (4) Wiesener, K. *Electrochim. Acta* **1986**, *31*, 1073.
- (5) Bezerra, C. W. B.; Zhang, L.; Lee, K. C.; Liu, H. S.; Marques, A. L. B.; Marques, E. P.; Wang, H. J.; Zhang, J. J. *Electrochim. Acta* **2008**, *53*, 4937.
- (6) Franke, R.; Ohms, D.; Wiesener, K. *J. Electroanal. Chem.* **1989**, *260*, 63.
- (7) van Veen, J. A. R.; Colijn, H. A.; van Baar, J. F. *Electrochim. Acta* **1988**, *33*, 801.
- (8) Scherson, D. A.; Gupta, S. L.; Fierro, C.; Yeager, E. B.; Kordesch, M. E.; Eldridge, J.; Hoffman, R. W.; Blue, J. *Electrochim. Acta* **1983**, *28*, 1205.
- (9) van der Putten, A.; Elzing, A.; Visscher, W.; Barendrecht, E. *J. Electroanal. Chem.* **1986**, *205*, 233.
- (10) Gupta, S.; Tryk, D.; Bae, I.; Aldred, W.; Yeager, E. *J. Appl. Electrochem.* **1989**, *19*, 19.
- (11) Ohms, D.; Herzog, S.; Franke, R.; Neumann, V.; Wiesener, K.; Gamburzev, S.; Kaisheva, A.; Iliev, I. *J. Power Sources* **1992**, *38*, 327.
- (12) Alves, M. C. M.; Dodelet, J. P.; Guay, D.; Ladouceur, M.; Tourillon, G. *J. Phys. Chem.* **1992**, *96*, 10898.
- (13) Li, W. M.; Yu, A. P.; Higgins, D. C.; Llanos, B. G.; Chen, Z. W. *J. Am. Chem. Soc.* **2010**, *132*, 17056.
- (14) Faubert, G.; Lalonde, G.; Cote, R.; Guay, D.; Dodelet, J. P.; Weng, L. T.; Bertrand, P.; Denes, G. *Electrochim. Acta* **1996**, *41*, 1689.
- (15) Lefevre, M.; Proietti, E.; Jaouen, F.; Dodelet, J. P. *Science* **2009**, *324*, 71.
- (16) Li, X.; Popov, B. N.; Kawahara, T.; Yanagi, H. *J. Power Sources* **2011**, *196*, 1717.
- (17) Wu, G.; More, K. L.; Johnston, C. M.; Zelenay, P. *Science* **2011**, *332*, 443.
- (18) Fuhrmann, A.; Wiesener, K.; Iliev, I.; Gamburzev, S.; Kaisheva, A. *J. Power Sources* **1981**, *6*, 69.
- (19) Lefevre, M.; Dodelet, J. P.; Bertrand, P. *J. Phys. Chem. B* **2000**, *104*, 11238.
- (20) Lalonde, G.; Cote, R.; Guay, D.; Dodelet, J. P.; Weng, L. T.; Bertrand, P. *Electrochim. Acta* **1997**, *42*, 1379.
- (21) Jaouen, F.; Lefevre, M.; Dodelet, J. P.; Cai, M. *J. Phys. Chem. B* **2006**, *110*, 5553.
- (22) Charreter, F.; Jaouen, F.; Ruggeri, S.; Dodelet, J. P. *Electrochim. Acta* **2008**, *53*, 2925.
- (23) Matter, P. H.; Zhang, L.; Ozkan, U. S. *J. Catal.* **2006**, *239*, 83.
- (24) Bron, M.; Fiechter, S.; Hilgendorff, M.; Bogdanoff, P. *J. Appl. Electrochem.* **2002**, *32*, 211.
- (25) Lalonde, G.; Faubert, G.; Cote, R.; Guay, D.; Dodelet, J. P.; Weng, L. T.; Bertrand, P. *J. Power Sources* **1996**, *61*, 227.
- (26) Subramanian, N. P.; Kumaraguru, S. P.; Colon-Mercado, H.; Kim, H.; Popov, B. N.; Black, T.; Chen, D. A. *J. Power Sources* **2006**, *157*, 56.
- (27) Liu, G.; Li, X. G.; Ganesan, P.; Popov, B. N. *Electrochim. Acta* **2010**, *55*, 2853.
- (28) Choi, J.; Hsu, R.; Chen, Z. *J. Phys. Chem. C* **2010**, *114*, 8048.
- (29) Chung, H. T.; Johnston, C. M.; Artyushkova, K.; Ferrandon, M.; Myers, D. J.; Zelenay, P. *Electrochem. Commun.* **2010**, *12*, 1792.
- (30) Bambagioni, V.; Bianchini, C.; Filippi, J.; Lavacchi, A.; Oberhauser, W.; Marchionni, A.; Moneti, S.; Vizza, F.; Psaro, R.; Dal Santo, V. *J. Power Sources* **2011**, *196*, 2519.
- (31) Wu, G.; Chen, Z.; Artyushkova, K.; Garzon, F. H.; Zelenay, P. *ECS Trans.* **2008**, *16*, 159.
- (32) Chung, H. T.; Johnston, C. M.; Zelenay, P. *ECS Trans.* **2009**, *24*, 485.
- (33) Bezerra, C. W. B.; Zhang, L.; Lee, K. C.; Liu, H. S.; Zhang, J. L.; Shi, Z.; Marques, A. L. B.; Marques, E. P.; Wu, S. H.; Zhang, J. J. *Electrochim. Acta* **2008**, *53*, 7703.
- (34) Nabae, Y.; Moriya, S.; Matsubayashi, K.; Lyth, S. M.; Malon, M.; Wu, L. B.; Islam, N. M.; Koshigoe, Y.; Kuroki, S.; Kakimoto, M. A.; Miyata, S.; Ozaki, J. *Carbon* **2010**, *48*, 2613.
- (35) Jaouen, F.; Dodelet, J. P. *J. Phys. Chem. C* **2007**, *111*, 5963.
- (36) Koslowski, U.; Herrmann, I.; Bogdanoff, P.; Barkschat, C.; Fiechter, S.; Iwata, N.; Takahashi, H.; Nishikori, H. *ECS Trans.* **2008**, *13*, 125.
- (37) Biddinger, E. J.; Ozkan, U. S. *Top. Catal.* **2007**, *46*, 339.
- (38) Matter, P. H.; Wang, E.; Arias, M.; Biddinger, E. J.; Ozkan, U. S. *J. Phys. Chem. B* **2006**, *110*, 18374.
- (39) Schulenburg, H.; Stankov, S.; Schunemann, V.; Radnik, J.; Dorbandt, I.; Fiechter, S.; Bogdanoff, P.; Tributsch, H. *J. Phys. Chem. B* **2003**, *107*, 9034.

(40) Meng, H.; Larouche, N.; Lefèvre, M.; Jaouen, F.; Stansfield, B.; Dodelet, J. *Electrochim. Acta* **2010**, *55*, 6450.

(41) Piela, B.; Olson, T. S.; Atanassov, P.; Zelenay, P. *Electrochim. Acta* **2009**, *55*, 7615.

(42) Moll, R. B.; Poziomek, E. J.; Mosher, W. A. *J. Org. Chem.* **1971**, *36*, 1056.

(43) Faubert, G.; Cote, R.; Dodelet, J. P.; Lefevre, M.; Bertrand, P. *Electrochim. Acta* **1999**, *44*, 2589.

(44) Jaouen, F. d. r.; Herranz, J.; Lefèvre, M.; Dodelet, J.-P.; Kramm, U. I.; Herrmann, I.; Bogdanoff, P.; Maruyama, J.; Nagaoka, T.; Garsuch, A.; Dahn, J. R.; Olson, T.; Pylypenko, S.; Atanassov, P.; Ustinov, E. A. *ACS Appl. Mater. Interfaces* **2009**, *1*, 1623.

(45) Arechederra, R. L.; Artyushkova, K.; Atanassov, P.; Minteer, S. D. *ACS Appl. Mater. Interfaces* **2010**, *2*, 3295.